



Experimental validation of multiscale modeling of indentation of suspended circular graphene membranes

Xiaoding Wei*, Jeffrey W. Kysar

Department of Mechanical Engineering, Columbia University, New York, NY 10027, United States

ARTICLE INFO

Article history:

Received 26 February 2012

Received in revised form 11 May 2012

Available online 10 July 2012

Keywords:

Graphene
Elastic instability
Phonon instability
Intrinsic strength

ABSTRACT

In recent studies, the in-plane elastic properties of graphene have been computed via Density Functional Theory (DFT) and expressed in the form of a higher-order continuum elastic constitutive model. The studies predict that graphene exhibits an anisotropic and non-linear elastic response at high strains. However, one study predicts that the rupture mechanism of graphene at its intrinsic strength is due to elastic instability whereas another study predicts the rupture mechanism at its intrinsic strength is due to phonon instability. In the present paper, we use the higher-order continuum elastic constitutive model within the context of the finite element method to simulate a set of experiments of the indentation of circular freestanding monatomic graphene membranes. There is a close correspondence between the measured and predicted measured force vs. displacement responses of indented graphene, providing experimental validation for the constitutive response. Further, there is a close correspondence between the measured and predicted breaking force of graphene via the elastic instability mechanism. Thus, the results suggest that the elastic instability precipitates failure of pristine graphene at its intrinsic strength, and also provides further experimental validation of the constitutive response.

© 2012 Elsevier Ltd. All rights reserved.

1. Introduction

Graphene, a two-dimensional sheet of sp^2 -bonded carbon atoms closely packed in a honeycomb crystal lattice, has potential applications (Chen et al., 2009; Geim, 2009; Lin et al., 2010; Van Noorden, 2006; Xu et al., 2009) in many fields and has been studied extensively since being isolated in 2004 (Novoselov et al., 2004). The extremely high surface area to volume ratio due to its two-dimensional structure makes graphene an excellent candidate material for detecting individual gas molecules (Schedin et al., 2007). Graphene has been used to make high-speed transistors and other electronic devices because of its outstanding electrical conductivity (Avouris et al., 2007; Chen et al., 2009; Lin et al., 2009, 2010). Furthermore, graphene has been proposed as an ideal candidate for light-weight high-performance composite materials (Stankovich et al., 2006) because of its extraordinary mechanical properties (Lee et al., 2008), such as high elastic modulus and the highest measured intrinsic strength of a known material. Such advanced applications require a fundamental understanding of the properties of graphene; in this paper we concentrate on the mechanical properties.

A recent set of experiments (Lee et al., 2008) probed the elastic properties as well as the *intrinsic strength* of graphene, which is the stress at which graphene fails in the absence of any defects. The geometry of the experimental configuration is illustrated in Fig. 1a. The substrate for the experiments was a silicon wafer with a 300 nm SiO_2 epilayer. An array of circular wells with diameters either of 1 μm or 1.5 μm was etched into the substrate to a depth of 500 nm. Monolayer graphene films were deposited over the array of holes via manual exfoliation from a graphite source. Two diamond AFM tips, each with a different radius, were used to deflect the center of the monolayer graphene films. Since the indenters had a spherical cap, the highest stress state in the graphene is expected to be immediately under the center of the indenter tip where the state of stress is expected to be equibiaxial tension. The force vs. displacement response of the deformed graphene is a function of the diameter of the suspended graphene film, but is insensitive to the AFM indenter tip radius. On the other hand, the force at which the monolayer graphene films ruptured is a function of the AFM indenter tip radius, but is insensitive to the diameter of the suspended graphene film. The radii of the two diamond indenter tips were 16.5 nm and 27.5 nm radius, which led to breaking forces, respectively of 1.8 μN and 2.9 μN as averaged over 23 different specimens.

Graphene is a brittle material, so the probability distribution of the experimental breaking forces was expected to be a Weibull distribution. However, the Weibull modulus obtained from the

* Corresponding author. Present address: Department of Mechanical Engineering, Northwestern University, 2145 Sheridan Rd., Evanston, IL 60208-3111, United States.

E-mail address: x-wei@northwestern.edu (X. Wei).

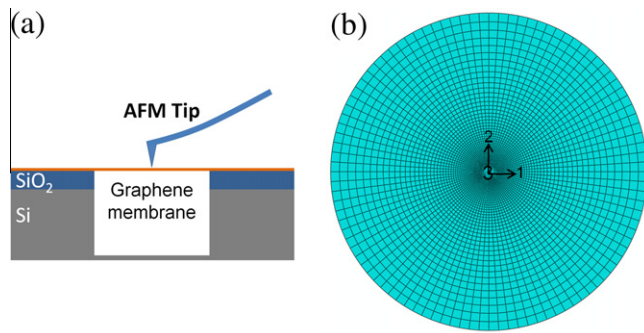


Fig. 1. (a): Schematic of Atomic Force Microscope (AFM) nanoindentation test on circular suspended graphene film performed in Lee et al. (2008); (b): Mesh of 1- μm -diameter graphene membrane with zigzag direction parallel to x_1 -axis and armchair direction parallel to x_2 -axis.

experimental values was an order of magnitude higher than the Weibull modulus measured both from the fracture of carbon nanotubes as well as from multiple length scale simulations of the deformation of defect-containing graphene sheets (see (Lee et al., 2008) for full discussion of Weibull modulus from the measurements). Given the very high value of Weibull modulus, it was postulated that graphene membranes ruptured in the absence of any defects. Thus, the stress state in the graphene films achieved the intrinsic strength of graphene at its point of failure. That the breaking force distribution was well approximated by a Gaussian distribution—indicating only random variations in the measured breaking force—is consistent with this interpretation.

Several authors have considered the intrinsic strength of graphene from a theoretical perspective (Khare et al., 2007; Kudin et al., 2001; Liu et al., 2007; Marianetti and Yevick, 2010; Van Lier et al., 2000; Wei et al., 2009). With regard to the equibiaxial stress state achieved under the indenter tip, Wei et al. (2009) employed density Functional Theory (DFT) and found the intrinsic strength of graphene to be achieved at a nominal strain of approximately 0.225, beyond which the material will rupture due to elastic instability. A recent report by Marianetti and Yevick (2010) based also on DFT calculations suggest that under an equibiaxial strain state, graphene will fail at a nominal strain of 0.151, before the elastic instability. Both first principles studies assumed a temperature of absolute zero as well as homogeneous in-plane deformation states. However, Marianetti and Yevick (2010) used a larger unit cell in their calculations that allows the activation of a phonon instability in a soft K_1 mode that is suppressed in the smaller unit cells of Wei et al. (2009). Otherwise, the elastic response up to the point of failure was identical in the two studies. Therefore, investigating the mechanical responses of graphene in the nanoindentation tests provides the opportunity to evaluate the instability mode that precipitates failure.

Multiple length scale constitutive models of graphene have recently been developed to describe its mechanical behavior under arbitrary in-plane deformation by fitting the strain energy density functions calculated from atomistic methods to higher-order polynomial approximations of the strain energy density function that account for the symmetries of the graphene atomic lattice (Cadelano et al., 2009; Wei et al., 2009). For example, Cadelano et al. (2009) combined continuum elasticity theory and tight-binding atomistic calculations to obtain a nonlinear elastic description for in-plane deformation in which the elastic strain energy density is expanded in a Taylor series truncated beyond the third-order term. The resulting formulation—with five independent elastic constants—provides a reasonable description of the behavior of graphene, but the behavior at both small strains and finite strains was not reproduced simultaneously with sufficient fidelity to allow

investigation of the rupture of graphene at high strains (Lee et al., 2008). Independently, Wei et al. (2009) performed *ab initio* calculations on graphene and derived a more general form of the continuum elastic strain energy density function that includes fourth- and fifth-order terms in strain, which will be discussed in detail below. Lu and Huang (2009) have derived a continuum framework that accounts for both in-plane and bending contributions to the elastic strain energy function, as well as terms that couple the in-plane and bending contributions.

The goal of this paper is threefold. First, we implement a multiple length scale, fifth-order non-linear continuum description of the elastic properties of graphene into the commercial finite element code, ABAQUS (SIMULIA, 2009) in the form of a user material (UMAT) subroutine. The UMAT is valid under arbitrary deformation states for which the radius of curvature of the deformed graphene is significantly larger than the in-plane interatomic spacing of the carbon atoms. Second, we simulate a set of indentation experiments (Lee et al., 2008) of freestanding monatomic graphene layers suspended over circular wells. Third, we demonstrate a very close correspondence between the calculated results and experimental results of both the force vs. displacement response of the indented graphene films as well as the breaking force of the graphene films. The results demonstrate that the stress in the film approached the intrinsic strength of graphene and failed due to elastic instability.

This paper is organized as follows. In Section 2 we review the multiple length scale stress–strain constitutive formulation of graphene (Wei et al., 2009). In Section 3, we describe the implementation of the constitutive formation into a user material (UMAT) subroutine. In Section 4, we describe the implementation of a small degree of phenomenological viscosity added to the constitutive model to enhance stability under conditions of strain softening. The details and results of the simulation of the indented suspended circular graphene films are discussed in Section 5. Finally, in Section 6, we discuss experimental validation of the constitutive relations as well as the mode of failure instability by highlighting the close correspondence of the simulation results to the experimental results.

2. Multiple length scale non-linear, anisotropic elastic constitutive model of graphene

A material that deforms in a thermodynamically reversible sense is said to exhibit elastic constitutive behavior. Such a response is predicated upon the existence of a strain energy density potential function that stores and releases energy associated with deformation. The strain energy density potential, denoted here as Φ , is a scalar function of the elastic strain.

As discussed in Wei et al. (2009), the elastic strain energy density can be expanded in a Taylor series in terms of powers of strain as

$$\Phi = \frac{1}{2!} C_{IJ} \eta_I \eta_J + \frac{1}{3!} C_{IJK} \eta_I \eta_J \eta_K + \frac{1}{4!} C_{IJKL} \eta_I \eta_J \eta_K \eta_L + \frac{1}{5!} C_{IJKLM} \eta_I \eta_J \eta_K \eta_L \eta_M + \dots, \quad (1)$$

where the Lagrangian strain, η_i , is chosen as the strain measure and the Voigt notation (Nye, 1985) is employed for subscripts: $11 \rightarrow 1$, $22 \rightarrow 2$, $33 \rightarrow 3$, $23 \rightarrow 4$, $32 \rightarrow 4$, $13 \rightarrow 5$, $31 \rightarrow 5$, $12 \rightarrow 6$, $21 \rightarrow 6$ (N.B. for strain, $\eta_4 = 2\eta_{23}$, $\eta_5 = 2\eta_{31}$, $\eta_6 = 2\eta_{12}$). Each higher-order elastic modulus tensor in Eq. (1) is denoted as C , and the number of subscripts indicates the order of the elastic constants, so the second-order elastic constants (SOEC) are components of C_{IJ} , the third-order elastic constants (TOEC) are components of C_{IJK} , the fourth-order elastic constants (FOEC) are components of C_{IJKL} , and

fifth-order elastic constants (FFOEC) are components of C_{ijklm} ; the tensors are fourth-, sixth-, eighth- and tenth-rank tensors, respectively. For graphene under an arbitrary in-plane deformation state, the only non-zero components of the Lagrangian strain tensor are η_1 , η_2 , and η_6 , which are according to the Voigt notation, $\eta_1 = \eta_{11}$, $\eta_2 = \eta_{22}$, and $\eta_6 = 2\eta_{12}$.

The stress associated with a given deformation state is determined from derivatives of the elastic strain energy density as follows

$$\begin{aligned} \Sigma_i &= \frac{\partial \Phi}{\partial \eta_i} \\ &= C_{ij} \eta_j + \frac{1}{2!} C_{ijkl} \eta_j \eta_k + \frac{1}{3!} C_{ijklm} \eta_j \eta_k \eta_l + \frac{1}{4!} C_{ijklmn} \eta_j \eta_k \eta_l \eta_m \\ &\quad + \dots \end{aligned} \quad (2)$$

with the second Piola–Kirchhoff stress tensor, Σ_i , work conjugate to the Lagrangian strain. For graphene, the only non-zero components of the stress tensor are, employing the Voigt notation,

$$\Sigma_1 = \Sigma_{11}, \quad \Sigma_2 = \Sigma_{22}, \quad \text{and} \quad \Sigma_6 = \Sigma_{12}.$$

From symmetry of the graphene atomic lattice, there are two independent elastic constants in the SOEC tensor, three in the TOEC tensor, four in the FOEC tensor, and five in the FFOEC tensor, respectively, for a total of fourteen independent elastic constants (Wei et al., 2009). The non-zero independent components for the high order elastic constant tensors are listed in Table 1 with dimensions of N/m suitable for a two-dimensional material; the values of the dependent components are listed in Wei et al. (2009). In the reference Cartesian coordinate system, the x_1 -axis is parallel to the graphene's zigzag direction and the x_2 -axis is parallel to the armchair direction, as in Fig. 2. The two independent second-order elastic constants determine the linear elastic behavior of graphene. One or more odd-order terms are necessary for a peak stress to exist in the stress–strain response.

In previous DFT calculations (Wei et al., 2009), a two-atom primitive cell was used. Periodic boundary conditions were applied and the out-of-plane dimension of the primitive cell was maintained at 15 Å to simulate an isolated monolayer graphene. The contribution of bending to the strain energy density of the primitive cell due to bending was assumed negligible as compared to the in-plane strain contribution. All the DFT calculations assumed zero temperature using the DFT code, Vienna *ab initio* simulation package (VASP) (Kresse and Furthmuller, 1996).

Three deformation states were investigated using the DFT calculations. One is a state of uniaxial strain in the zigzag direction, such that $\eta_1 \geq 0$, $\eta_2 = 0$, $\eta_6 = 0$, with reference to Fig. 2. The calculated stress state is plotted using symbols in Fig. 3, where Σ_1^{zig} develops due to the extensional strain along the x_1 -axis and Σ_2^{zig} develops due to the lateral strain constraints along the x_2 -axis. The second deformation state is uniaxial strain in the armchair direction for which $\eta_1 = 0$, $\eta_2 \geq 0$, $\eta_6 = 0$, with reference to Fig. 2. The stress state is plotted using symbols in Fig. 3 where Σ_2^{arm} develops due to the extensional strain along the x_2 -axis and Σ_1^{arm} develops due to the lateral strain constraints along the x_1 -axis. The third

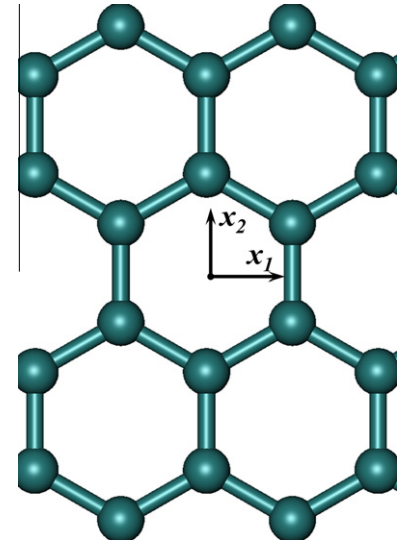


Fig. 2. Schematic of Cartesian coordinate system for higher order elastic constants of graphene lattice in this study- x_1 -axis is parallel to zigzag direction and x_2 -axis is parallel to armchair direction.

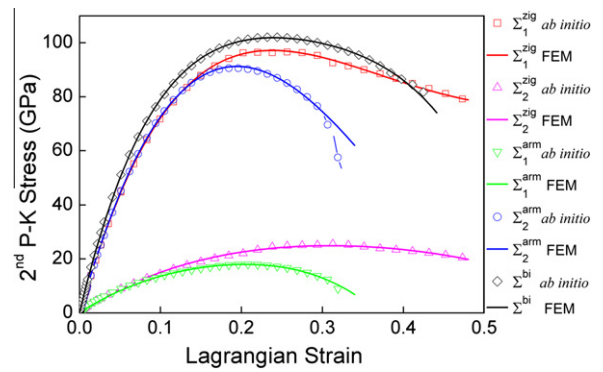


Fig. 3. Comparison of stress–strain responses for graphene under plane strain tension in armchair and zigzag directions and equibiaxial tension obtained from FEM simulation and *ab initio* calculations in Wei et al. (2009). Superscripts represent the direction in which tension is applied and subscripts represent the second P-K stress components using Voigt notation.

deformation state is equibiaxial strain for which $\eta_1 = \eta_2 = \eta \geq 0$ and $\eta_6 = 0$, with reference to Fig. 2. The resulting stress state is plotted using symbols in Fig. 3 as $\Sigma_1 = \Sigma_2 = \Sigma^{bi}$, $\Sigma_6 = 0$. For each of the three deformation states, the strain energy density and the elastic response were calculated for extensional strains up to a value of 0.32. These deformation states were chosen because their continuum descriptions invoke, together, all fourteen elastic constants, as discussed in Wei et al. (2009).

The values of the fourteen elastic constants were determined by least-squares fitting the elastic constitutive relations to the DFT calculations. The resulting elastic constants are in Table 1. The solid curves in Fig. 3 indicate best fit of the fifth-order continuum description. It is instructive to note that the anisotropy inherent in the finite deformation response does not manifest itself until after a strain level of about 15%, notwithstanding that the elastic response becomes noticeably nonlinear beyond a strain of about 5%.

3. Finite element implementation into ABAQUS

In this section we describe the implementation of the elastic constitutive model as a user material (UMAT) in the commercial

Table 1

Non-zero independent components for the SOEC, TOEC, FOEC and FFOEC tensors of graphene (Wei et al., 2009).

SOEC (N/m)	TOEC (N/m)	FOEC (N/m)	FFOEC (N/m)
$C_{11}^{(2D)} = 358.1$	$C_{111}^{(2D)} = -2817$	$C_{1111}^{(2D)} = 13416.2$	$C_{11111}^{(2D)} = -31383.8$
$C_{12}^{(2D)} = 60.4$	$C_{112}^{(2D)} = -337.1$	$C_{1112}^{(2D)} = 759$	$C_{11112}^{(2D)} = -88.4$
	$C_{222}^{(2D)} = -2693.3$	$C_{1122}^{(2D)} = 2582.8$	$C_{11122}^{(2D)} = -12960.5$
		$C_{2222}^{(2D)} = 10358.9$	$C_{12222}^{(2D)} = -13046.6$
			$C_{22222}^{(2D)} = -33446.7$

finite element code, ABAQUS (SIMULIA, 2009). The constitutive model was developed under the assumption of an in-plane deformation state, so the out-of-plane bending stiffness is assumed to be zero, despite graphene having a non-zero bending stiffness (Wei et al., 2009). Nonetheless the constitutive model is valid for deformation states for which out-of-plane rotations occur as long as the elastic strain energy induced by the bending deformation is much less than the elastic strain energy induced by the in-plane deformation. Thus, the UMAT is used specifically for membrane elements, which accounts for contributions to the elastic strain energy density from in-plane strains but neglects that from bending strains.

Since membranes typically have substantial of out-of-plane deformation, it is necessary to ensure that the stress–strain constitutive relationship is applied in such a way that it is frame invariant. ABAQUS achieves this by applying the constitutive relationship in a local coordinate frame that instantaneously rotates with the material—specifically at the Jaumann rate—at each integration point (e.g. Dunne and Petrinic, 2005). For the graphene UMAT, the zigzag direction of the graphene is always parallel to the local x_1 -axis, the armchair direction is always parallel to the local x_2 -axis and the local x_3 -axis coincides with the unit normal vector of the graphene.

For calculations at each increment of the simulation, ABAQUS passes into the UMAT subroutine the following quantities: total true strain, ε_i , at the beginning of the increment; true strain increment, $\Delta\varepsilon$, during the time increment; the Cauchy stress tensor, σ_i , at the beginning of the increment; and, the deformation gradient tensors at the beginning and the end of the increment, \mathbf{F}_i and \mathbf{F}_f (the subscript i represents initial, and f represents final, respectively). In turn, the UMAT subroutine calculates the material Jacobian matrix, defined as $\partial\Delta\sigma/\partial\Delta\varepsilon$ (e.g. Dunne and Petrinic, 2005), and also calculates the Cauchy stress tensor, σ_f , at the end of the increment. However, since the constitutive law for graphene given in Eq. (2) is in terms of the second Piola–Kirchhoff stress and the Lagrangian strain tensors, all calculation in the UMAT subroutine are in terms of second Piola–Kirchhoff stress and Lagrangian strain tensors, and proper conversions between the Cauchy stress and logarithmic strains quantities are made as required.

The Lagrangian strain tensors at the beginning and end of each time increment, $\boldsymbol{\eta}_i$ and $\boldsymbol{\eta}_f$, can be expressed as

$$\boldsymbol{\eta}_i = \frac{1}{2} (\mathbf{F}_i^T \mathbf{F}_i - \mathbf{I}) \quad \text{and} \quad \boldsymbol{\eta}_f = \frac{1}{2} (\mathbf{F}_f^T \mathbf{F}_f - \mathbf{I}), \quad (3)$$

where \mathbf{F}_i and \mathbf{F}_f are the initial and final deformation gradient tensors in the time increment, respectively. From the constitutive law given in Eq. (2), we express the material Jacobian matrix in terms of the second Piola–Kirchhoff stress and Lagrangian strain tensors as

$$\left[\frac{\partial\Delta\boldsymbol{\Sigma}}{\partial\Delta\boldsymbol{\eta}} \right]_{JJ} = \frac{\partial\Delta\boldsymbol{\Sigma}_I}{\partial\Delta\boldsymbol{\eta}_J} = C_{IJ} + C_{IJK}\eta_K + \frac{1}{2!}C_{IJKL}\eta_K\eta_L + \frac{1}{3!}C_{IJKLM}\eta_K\eta_L\eta_M. \quad (4)$$

It is of interest to note that unlike linear isotropic elastic materials, for which the material Jacobian matrix consists only of the first term in the right hand side of Eq. (4) (e.g. Dunne and Petrinic, 2005), the Jacobian matrix for graphene contains the higher order terms of the Lagrangian strain components. Thus, the Jacobian matrix for graphene depends on the current strain state of the material. The increment of the second Piola–Kirchhoff stress tensor is then expressed as

$$\Delta\boldsymbol{\Sigma} = \left[\frac{\partial\Delta\boldsymbol{\Sigma}}{\partial\Delta\boldsymbol{\eta}} \right] \Delta\boldsymbol{\eta}, \quad (5)$$

in which $\Delta\boldsymbol{\eta} = \boldsymbol{\eta}_f - \boldsymbol{\eta}_i$ is the Lagrangian strain increment during the time step. The second Piola–Kirchhoff stress tensor at the end of the time increment, $\boldsymbol{\Sigma}_1$, can be updated as

$$\boldsymbol{\Sigma}_f = \boldsymbol{\Sigma}_i + \Delta\boldsymbol{\Sigma} \quad (6)$$

where $\boldsymbol{\Sigma}_i$ is the second Piola–Kirchhoff stress tensor at the beginning of the time increment. To be consistent with the convention in ABAQUS, we also convert the second Piola–Kirchhoff stress tensor into the Cauchy stress tensor at the end of the UMAT subroutine. The updated Cauchy stress tensor, σ_f , at the end of the time increment is (e.g. Dunne and Petrinic, 2005)

$$\boldsymbol{\sigma}_f = \frac{1}{J} \mathbf{F}_f \boldsymbol{\Sigma}_f \mathbf{F}_f^T \quad (7)$$

where J is the determinant of the deformation gradient tensor, \mathbf{F}_f .

4. Snap-back instability, small viscosity and model verification

Numerical methods have computational difficulties in handling problems with significant strain softening (i.e. when the deformation of the material increases, the tangent stiffness of the system decreases). Since the constitutive behavior of graphene given in Eq. (2) has strain softening, convergence difficulties tend to occur during the Newton–Raphson iterations as the stress–strain response reaches a peak (or, the tangent stiffness approaches zero). This computation difficulty is known as the snap-back instability (Gao, 2006; Gao and Bower, 2004) (or called ‘Z’ or ‘S’-type instability), and the radius of convergence of the Newton–Raphson method may reduce to zero at the point of instability. Gao and Bower (2004) introduced a simple technique for avoiding convergence difficulties for such cases by introducing a small amount of viscosity in the constitutive model.

Adding a viscous term into the constitutive model in Eq. (2), a new constitutive law can be expressed as

$$\boldsymbol{\Sigma}_I = C_{IJ}\dot{\eta}_J + \frac{1}{2!}C_{IJK}\dot{\eta}_J\dot{\eta}_K + \frac{1}{3!}C_{IJKL}\dot{\eta}_J\dot{\eta}_K\dot{\eta}_L + \frac{1}{4!}C_{IJKLM}\dot{\eta}_J\dot{\eta}_K\dot{\eta}_L\dot{\eta}_M + D_{IJ}\dot{\eta}_J. \quad (8)$$

where $\dot{\eta}_J$ is the component of Lagrangian strain rate tensor, D_{IJ} is the viscoelastic constant tensor (with unit of $GPa \cdot s$), which is defined as

$$D_{IJ} = \mu C_{IJ} \quad (9)$$

in which μ is a viscosity-like parameter that has units of time. Applying the central difference operation on Eq. (8), yields

$$\begin{aligned} \boldsymbol{\Sigma}_I + \frac{\Delta\boldsymbol{\Sigma}_I}{2} = & C_{IJ} \left(\eta_J + \frac{\Delta\eta_J}{2} \right) + \frac{1}{2!}C_{IJK} \left(\eta_J + \frac{\Delta\eta_J}{2} \right) \left(\eta_K + \frac{\Delta\eta_K}{2} \right) \\ & + \frac{1}{3!}C_{IJKL} \left(\eta_J + \frac{\Delta\eta_J}{2} \right) \left(\eta_K + \frac{\Delta\eta_K}{2} \right) \left(\eta_L + \frac{\Delta\eta_L}{2} \right) \\ & + \frac{1}{4!}C_{IJKLM} \left(\eta_J + \frac{\Delta\eta_J}{2} \right) \left(\eta_K + \frac{\Delta\eta_K}{2} \right) \left(\eta_L + \frac{\Delta\eta_L}{2} \right) \left(\eta_M + \frac{\Delta\eta_M}{2} \right) \\ & + D_{IJ} \frac{\Delta\eta_J}{\Delta t}. \end{aligned} \quad (10)$$

where Δt is the time increment. Then the material Jacobian matrix in the UMAT subroutine takes the form

$$\begin{aligned} \left[\frac{\partial\Delta\boldsymbol{\Sigma}}{\partial\Delta\boldsymbol{\eta}} \right]_{JJ} = & C_{IJ} + C_{IJK} \left(\eta_K + \frac{\Delta\eta_K}{2} \right) \\ & + \frac{1}{2!}C_{IJKL} \left(\eta_K + \frac{\Delta\eta_K}{2} \right) \left(\eta_L + \frac{\Delta\eta_L}{2} \right) \\ & + \frac{1}{3!}C_{IJKLM} \left(\eta_K + \frac{\Delta\eta_K}{2} \right) \left(\eta_L + \frac{\Delta\eta_L}{2} \right) \left(\eta_M + \frac{\Delta\eta_M}{2} \right) \\ & + 2 \frac{D_{IJ}}{\Delta t}. \end{aligned} \quad (11)$$

The increment of the second Piola–Kirchhoff stress can be expressed as

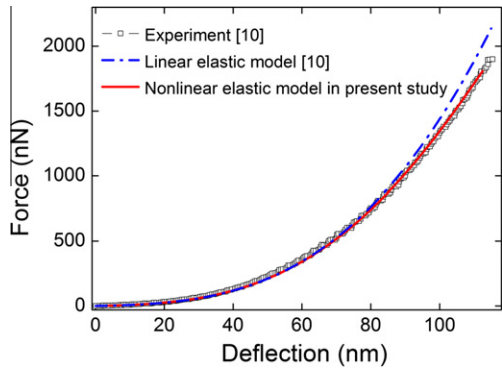


Fig. 4. Comparison of force-deflection responses obtained from experiments (hollow symbols), FEM simulation with linear elastic model (Lee et al., 2008), and FEM simulation with nonlinear elastic model in present study.

$$\begin{aligned} \Delta \Sigma_i = & 2C_{ij} \left(\eta_j + \frac{\Delta \eta_j}{2} \right) + C_{ijk} \left(\eta_j + \frac{\Delta \eta_j}{2} \right) \left(\eta_k + \frac{\Delta \eta_k}{2} \right) \\ & + \frac{1}{3} C_{ijkl} \left(\eta_j + \frac{\Delta \eta_j}{2} \right) \left(\eta_k + \frac{\Delta \eta_k}{2} \right) \left(\eta_l + \frac{\Delta \eta_l}{2} \right) \\ & + \frac{1}{12} C_{ijklm} \left(\eta_j + \frac{\Delta \eta_j}{2} \right) \left(\eta_k + \frac{\Delta \eta_k}{2} \right) \left(\eta_l + \frac{\Delta \eta_l}{2} \right) \left(\eta_m + \frac{\Delta \eta_m}{2} \right) \\ & + D_{ij} \frac{2\Delta \eta_j}{\Delta t} - 2[\Sigma_i]_l \end{aligned} \quad (12)$$

where Σ_i is the second Piola–Kirchhoff stress tensor at the beginning of the time increment. The magnitude of D_{ij} (or viscosity term, μ) must be sufficiently small to avoid sacrificing the accuracy of the constitutive law and but large enough to avoid the convergence difficulties. We combined Eqs. (11) and (12) with (6) and (7) to develop the UMAT.

To verify the continuum model implementation in the UMAT, we performed three simulations to compare with results obtained from *ab initio* calculations under three deformation states: uniaxial strain in the zigzag direction, uniaxial strain in the armchair direction and equibiaxial strain. A graphene flake with dimension of 1×1 nm was meshed with a total of 100 four-node linear quadrilateral membrane elements. The Newton–Raphson scheme was applied in the simulation with 1000 increments over a quasi-static load step. The stress–strain responses for graphene under the three deformation configurations obtained by finite element method match the stresses evaluated directly from the constitutive model (c.f. Fig. 3) to within a small fraction of a percent. Thus, for a sufficiently small viscosity parameter, μ , the continuum model implemented in ABAQUS is able to capture correctly the *ab initio* stress–strain responses of graphene at very little cost of computational accuracy.

5. Model validation by AFM indentation test

We now describe an implementation of the UMAT to simulate Atomic Force Microscope (AFM) nanoindentation experiments on

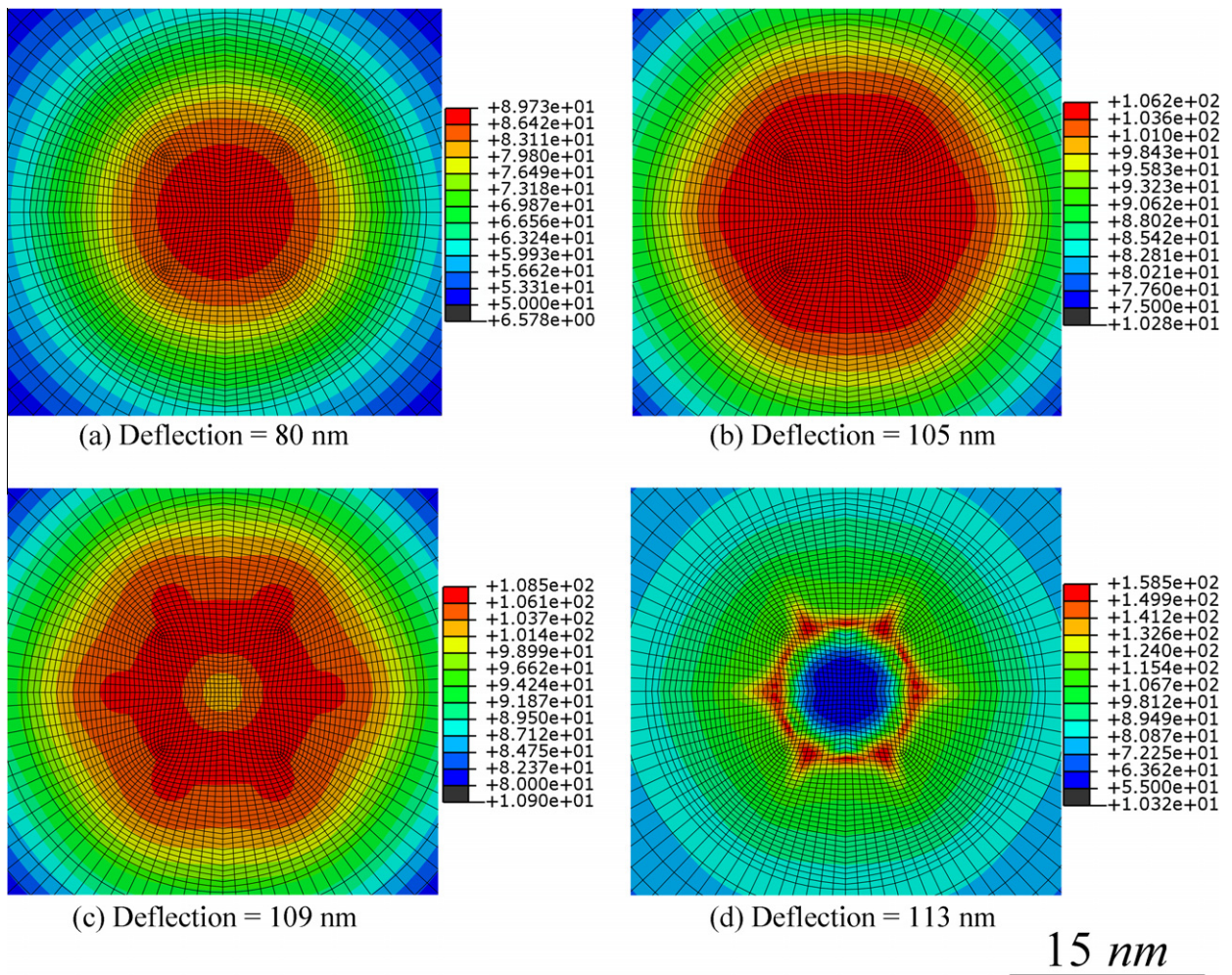


Fig. 5. Evolution of maximum in-plane principal Cauchy stress (GPa, assuming nominal thickness of 0.335 nm) at central region of the graphene during indentation.

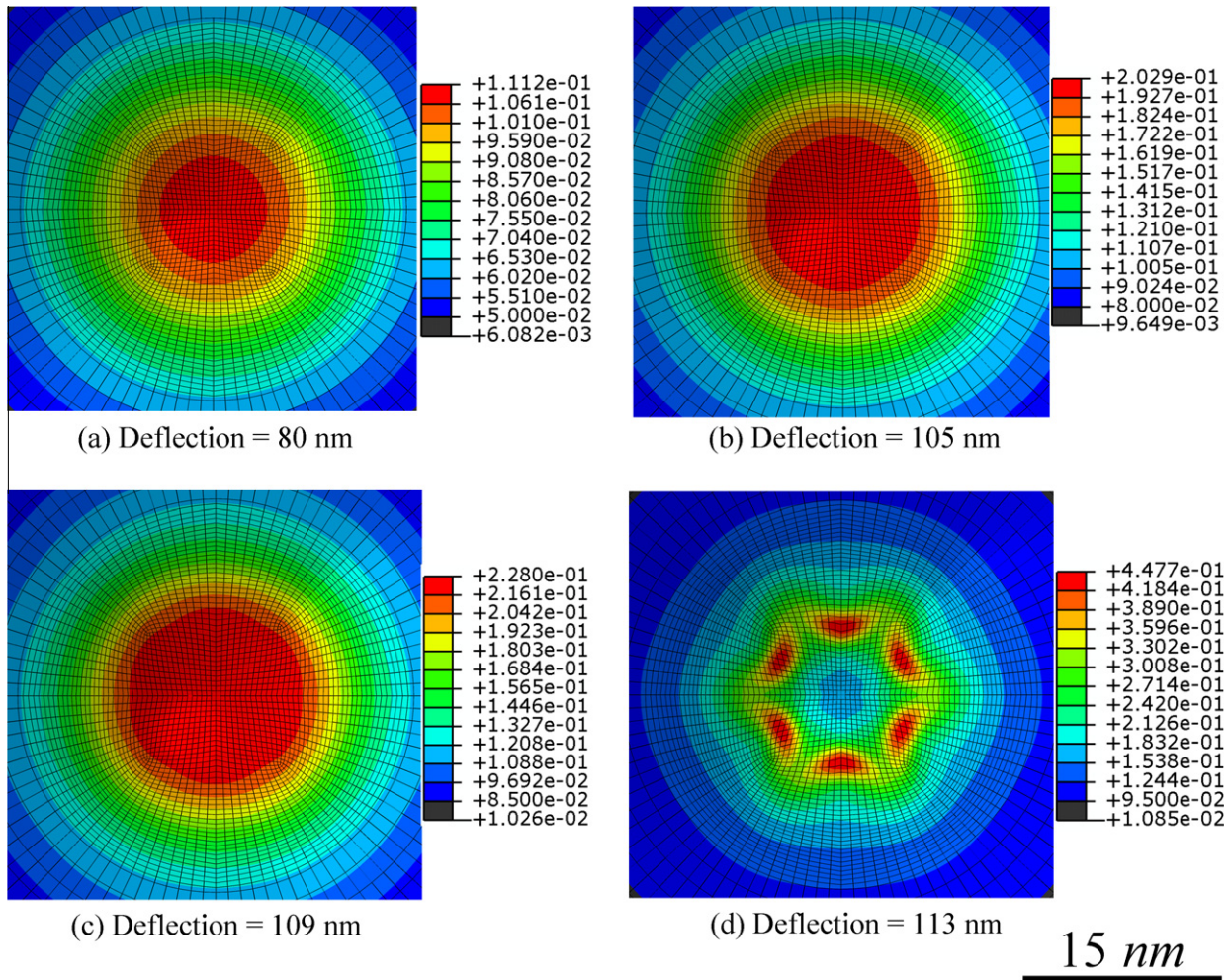


Fig. 6. Evolution of maximum in-plane principal logarithmic strain at central region of the graphene during indentation.

circular suspended graphene films. Since graphene has monatomic thickness it is considered to be a two-dimensional material with an indeterminable thickness, so that stress quantities are defined with units of force per length rather than units of stress per area. However, the finite element formulation requires membrane elements to have a prescribed effective thickness, which we arbitrarily choose to be $h = 0.335$ nm which is the interlayer spacing of graphite (Aljishi and Dresselhaus, 1982). In addition, the finite element formulation requires stress and the elastic constants to be effective three-dimensional quantities with units of force per area. Here we will denote the effective three-dimensional quantities with a superscript (3D). The relationship between the two-dimensional and three-dimensional stress quantities are, for the case of the second-order elastic constants, $C_{ij} = C_{ij}^{(3D)}h$. All other elastic constants as well as the stress components themselves follow the same relationship between intrinsic two-dimensional quantities and effective three-dimensional quantities necessary in the finite element formulation.

The freestanding $1 \mu\text{m}$ diameter graphene membrane is meshed with 16,270 four-node linear quadrilateral membrane elements as shown in Fig. 1b. The zigzag direction of the graphene is parallel to the x_1 -axis and the armchair direction is parallel to the x_2 -axis in the initial configuration. The central region of the graphene membrane has a higher mesh density: a total of 3374 elements within the inner 15 nm radius. The indenter tip is modeled as a frictionless spherical rigid body with radius of 16.5 nm, consistent with the smaller AFM tip used in the experiments. Before indenta-

tion, an initial uniform equibiaxial in-plane stress of 0.335 N/m (corresponds 1 GPa effective three-dimensional stress) is applied to the graphene membrane to compensate for the initial tension in the graphene due to the van der Waals interaction between graphene and the periphery of the well (Lee et al., 2008).

The position of the indenter tip is prescribed throughout the simulation, achieving a final indentation depth of 113 nm after 1000 time increments. The simulation becomes unstable as the tangent stiffness of the graphene reduces to near zero in the most highly stressed portion of the graphene directly under the indenter tip. We choose $\mu = 3.5 \times 10^{-3}$ s, which is the minimum value that enables the peak stress in the graphene to be achieved under the center of the indenter.

Fig. 5 shows the effective three-dimensional maximum in-plane principal Cauchy stress in units of GPa in the central region of the graphene at different indentation depths. For relatively small deformations (when deflection is less than 80 nm as shown in Fig. 5a), the graphene film shows an approximate equibiaxial strain response. That is, the mechanical response of graphene is approximately isotropic, even well into the nonlinear elastic regime. When the indentation depth increases to 105 nm (Fig. 5b), the graphene is seen to exhibit an anisotropic nonlinear elastic behavior, evidenced by the sixfold rotation symmetry of the stress state, which is consistent with the sixfold rotation symmetry of the graphene atomic lattice. At an indentation depth of 109 nm (Fig. 5c), the central point of the graphene begins to exhibit a strain softening because the strain in the graphene at that point is beyond

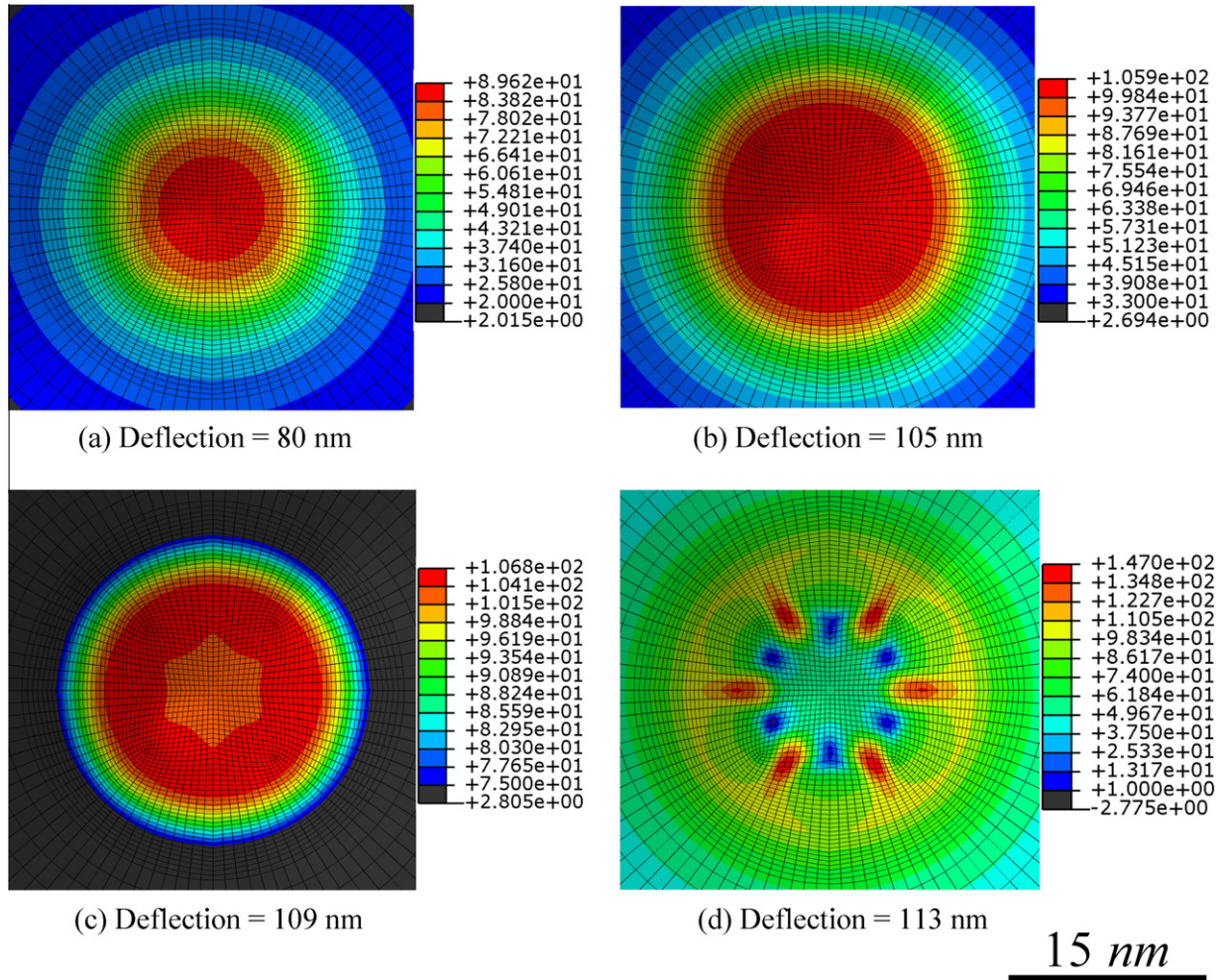


Fig. 7. Evolution of minimum in-plane principal Cauchy stress (GPa, assuming nominal thickness of 0.335 nm) at central region of the graphene during indentation.

that which corresponds to the peak, or intrinsic, stress in the constitutive response. Clearly the strain softening will lead to elastic instability with further deformation. This is seen at the final increment in the simulation after which the solver failed to converge to an equilibrium solution; the vicinity of the film center shows a clear sixfold symmetric pattern of stress localization (Fig. 5d).

The maximum stresses in Fig. 5b and c are essentially the same. Thus the effective viscosity played a negligible role determining the stress state prior to severe strain localization. In Fig. 5d, the stress is highly localized in the zigzag directions, indicating deformation instability. However, the maximum stress in Fig. 5d is significantly higher than the intrinsic stress calculated from DFT, so it is apparent that the effective velocity plays a non-negligible role in the evolution from Fig. 5c and d. Thus, the simulations predict the graphene membrane to fail at some indentation depth between the 109 nm of Fig. 5c and the 113 nm of Fig. 5d. The breaking force estimated by the FEM simulations on 1- μm -diameter graphene membranes indented by the diamond probe with tip radius of 16.5 nm is 1.818 μN , which is consistent with the mean value of the experimental breaking force of 1.8 μN to within the experimental uncertainty (Lee et al., 2008). The force on the indenter increases by about 0.1 μN in the simulation between those two states in Fig. 5c and d.

The force–deflection response from the FEM simulation with the 16.5 nm tip is shown in Fig. 4. For comparison, one experimental result as well as the result from the FEM simulation with a linear elastic model (Lee et al., 2008) are also included. The force–

deflection response given by the FEM simulations with the nonlinear elastic model is consistent with the experimental result. Furthermore, it is of interest to note that at large deformation (deflection of the membrane beyond 80 nm), the graphene membrane starts to show the nonlinear elastic behavior, which is successfully captured by the constitutive model. The linear elastic model describes well the mechanical response of graphene for small deflection; however, it exhibits relatively large deviation for the responses at large deformation.

The maximum in-plane principal logarithmic strain, minimum in-plane principal Cauchy stress (GPa), minimum in-plane principal logarithmic strain fields at the central region of the graphene at the same four time steps are shown in Figs. 6–8, respectively. All demonstrate the development of anisotropic stress–strain responses at large deformation and highlight the stress localizations when graphene is loaded to the breaking point.

Fig. 9 shows the distribution of the second Piola–Kirchhoff stress components, Σ_1 and Σ_2 , along the radius in zigzag and armchair, respectively, at an indentation depth of 109 nm. At this point the central region of the graphene film has been deformed enough such that these two stress distributions clearly demonstrate anisotropic stress–strain response and strain softening. However, the plot suggests that in regions away from the center of the film, the stress–strain response is still approximately isotropic. Furthermore, the inset of Fig. 9 confirms that the center point of the film is still in equibiaxial strain state ($\Sigma_1 \approx \Sigma_2$).

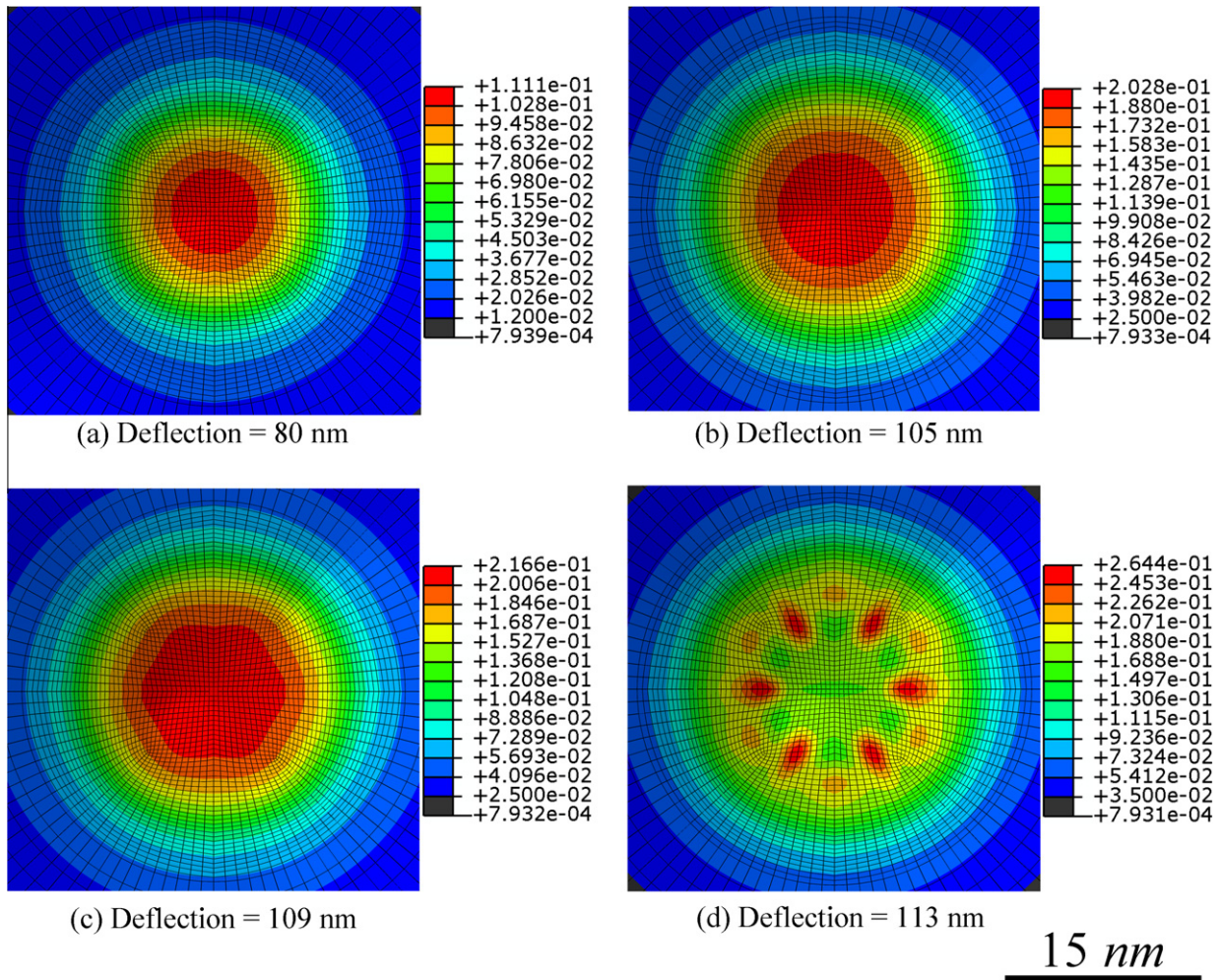


Fig. 8. Evolution of minimum in-plane principal logarithmic strain at central region of the graphene during indentation.

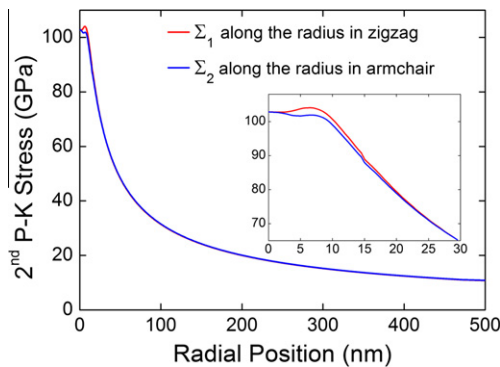


Fig. 9. Distribution of second P-K stress components, Σ_1 and Σ_2 (GPa, assuming nominal thickness of 0.335 nm using Voigt notation) at indentation depth of 109 nm along the radius in armchair and zigzag direction, respectively. Inset figure highlights anisotropy and strain softening at region near film center.

In addition, another simulation was performed on the same 1- μm -diameter graphene indented with the larger indenter (tip radius of 27.5 nm) used in Lee et al. (2008). The predicted breaking force of 2.988 μN for the larger tip, agrees with the mean experimental value of 2.9 μN within the experimental uncertainty (Lee et al., 2008).

A very close correspondence between the calculated results and experimental results of both the force vs. displacement response of

the indented graphene films as well as the breaking force of the graphene films strongly suggests the failure is caused by the elastic instability. However, we also investigate whether the experimental result is consistent with the phonon instability (Marianetti and Yevick, 2010). If failure would have occurred at equibiaxial strain of 0.151, consistent with the phonon instability, the breaking forces would have been 0.935 μN and 1.558 μN , for 16.5 nm and 27.5 nm radius tips, respectively. These discrepancies are far greater than the experimental uncertainty, so the phonon instability apparently is not activated in the experiments.

6. Discussion and conclusions

In the present study, the fifth-order nonlinear elastic constitutive law for graphene (Wei et al., 2009) has been reviewed and the implementation of the nonlinear elastic constitutive law into the commercial finite element code, ABAQUS, through the user defined material subroutine has been discussed. The computational difficulty (snap-back instability) due to graphene's strain-softening at large deformation has been overcome by introducing a small viscosity into the nonlinear elastic constitutive model. The capability of the modified nonlinear elastic constitutive model to describe the mechanical response of graphene under a general deformation configuration has been validated by applying the UMAT subroutine into the finite element simulations of the nanoindentation tests on free-standing graphene films. There is a high degree of consistency

between the numerical and experimental results; thus the nonlinear continuum model is able to capture the mechanical response of graphene at strains above 5% when the nonlinearity becomes important as well as at strains above 15% when the elastic properties become appreciably anisotropic. Furthermore, the finite element simulation based on the nonlinear elastic model provides details on the stress and strain fields within graphene under the influence of a spherical indenter.

In addition, the UMAT subroutine reveals the detailed stress and strain configurations in the graphene membrane. The simulation results demonstrate that rupture in the central region of the graphene in the indentation tests initiates in the strain-softening stage at a strain of approximately 0.228 after having passed the maximum strength. This suggests that the failure mechanism is due to an elastic instability rather than the phonon instability in soft K_1 mode (Marianetti and Yevick, 2010) which would have occurred at a smaller magnitude indentation force than measured in the experiments. In addition to assuming deformation at the temperature of absolute zero, it is important to note that the DFT computations assumed freestanding graphene under a homogeneous in-plane deformation state, whereas experimentally, the graphene and the diamond indenter tip are in contact and the deformation state is heterogeneous with modest out-of-plane bending. It is possible that the phonon instability may be suppressed under such conditions. Therefore, further theoretical and experimental studies are essential to validate the proposed failure mechanisms. For example, one could perform atomistic modeling at room temperature to investigate the failure modes of graphene in various strain states; and bulge test experiments (Vlassak and Nix, 1992; Wei et al., 2007; Xiang et al., 2006) can serve as an alternative to nanoindentation in order to eliminate the possible indenter-to-sample interactions.

Acknowledgement

The authors gratefully acknowledge support from NSF-CMMI-0927891 and AFOSR FA9550-09-1-0048.

References

- Aljishi, R., Dresselhaus, G., 1982. Lattice-dynamical model for graphite. *Physical Review B* 26, 4514–4522.
- Avouris, P. et al., 2007. Carbon-based electronics. *Nature Nanotechnology* 2, 605–615.
- Cadelano, E. et al., 2009. Nonlinear elasticity of monolayer graphene. *Physical Review Letters* 102, 235502.
- Chen, C. et al., 2009. Performance of monolayer graphene nanomechanical resonators with electrical readout. *Nature Nanotechnology* 4, 861–867.
- Dunne, F., Petrinic, N., 2005. *Introduction to Computational Plasticity*. Oxford University Press.
- Gao, Y., 2006. An implicit finite element method for simulating inhomogeneous deformation and shear bands of amorphous alloys based on the free-volume model. *Modelling and Simulation in Materials Science and Engineering* 14, 1329.
- Gao, Y., Bower, A., 2004. A simple technique for avoiding convergence problems in finite element simulations of crack nucleation and growth on cohesive interfaces. *Modelling and Simulation in Materials Science and Engineering* 12, 453–463.
- Geim, A.K., 2009. Graphene: status and prospects. *Science* 324, 1530–1534.
- Khare, R. et al., 2007. Coupled quantum mechanical/molecular mechanical modeling of the fracture of defective carbon nanotubes and graphene sheets. *Physical Review B* 75, 075412.
- Kresse, G., Furthmüller, J., 1996. Efficiency of ab-initio total energy calculations for metals and semiconductors using a plane-wave basis set. *Computational Materials Science* 6, 15–50.
- Kudin, K.N. et al., 2001. C_2F , BN, and C nanoshell elasticity from ab initio computations. *Physical Review B* 64, 235406.
- Lee, C. et al., 2008. Measurement of the elastic properties and intrinsic strength of monolayer graphene. *Science* 321, 385.
- Lin, Y.-M. et al., 2010. 100-GHz transistors from wafer-scale epitaxial graphene. *Science* 327, 662.
- Lin, Y.M. et al., 2009. Operation of graphene transistors at gigahertz frequencies. *Nano Letters* 9, 422–426.
- Liu, F. et al., 2007. Ab initio calculation of ideal strength and phonon instability of graphene under tension. *Physical Review B*, 76.
- Lu, Q., Huang, R., 2009. Nonlinear mechanics of single-atomic-layer graphene sheets. *International Journal of Applied* 1, 443–467.
- Marianetti, C.A., Yevick, H.G., 2010. Failure mechanisms of graphene under tension. *Physical Review Letters* 105, 245502.
- Novoselov, K.S. et al., 2004. Electric field effect in atomically thin carbon films. *Science* 306, 666–669.
- Nye, J.F., 1985. *Physical Properties of Crystals*. Oxford.
- Schedin, F. et al., 2007. Detection of individual gas molecules adsorbed on graphene. *Nature Materials* 6, 652–655.
- SIMULIA, 2009. *ABAQUS 6.7 User's Manual*, 6.7-1 ed. ABAQUS Inc., Pawtucket, RI.
- Stankovich, S. et al., 2006. Graphene-based composite materials. *Nature* 442, 282–286.
- Van Lier, G. et al., 2000. Ab initio study of the elastic properties of single-walled carbon nanotubes and graphene. *Chemical Physics Letters* 326, 181–185.
- Van Noorden, R., 2006. Moving towards a graphene world. *Nature* 442, 228–229.
- Vlassak, J., Nix, W.D., 1992. A new bulge test technique for the determination of Young's modulus and Poisson's ratio of thin films. *Journal of Materials Research* 7, 3242–3249.
- Wei, X. et al., 2009. Nonlinear elastic behavior of graphene: Ab initio calculations to continuum description. *Physical Review B* 80, 205407.
- Wei, X. et al., 2007. Plane-strain bulge test for nanocrystalline copper thin films. *Scripta Materialia* 57, 541–544.
- Xiang, Y. et al., 2006. The mechanical properties of freestanding electroplated Cu thin films. *Journal of Materials Research* 21, 1607–1618.
- Xu, X. et al., 2009. Photo-thermoelectric effect at a graphene interface junction. *Nano Letters* 10, 562–566.